Surface Science 604 (2010) 692–700

Contents lists available at ScienceDirect

Surface Science

journal homepage: www.elsevier.com/locate/susc

Investigation of the structural and dynamical properties of the (001) surface of $LiCu_2O_2$

Yangyang Yao [a], Xuetao Zhu [a], H.C. Hsu [b], F.C. Chou [b], M. El-Batanouny [a,*]

[a] Physics Department, Boston University, Boston, MA 02215, United States
[b] Center of Condensed Matter Sciences, National Taiwan University, Taipei 10617, Taiwan

ARTICLE INFO

Article history:
Received 19 October 2009
Accepted for publication 22 January 2010
Available online 4 February 2010

Keywords:
$LiCu_2O_2$
Helium atom scattering
Surface structure
Surface dynamics
Surface phonons

ABSTRACT

We report on studies of the structure and dynamics of the (001) surface of single crystal $LiCu_2O_2$, investigated by He beam scattering at room temperature, and with lattice-dynamical models. The best fit surface corrugation to measured diffraction patterns shows that the surface termination is exclusively a $Li^{1+}Cu^{2+}O^{2-}$ plane. Lattice dynamics fits to inelastic He scattering spectra reveal the presence of two low-lying surface phonon modes, identified with the motion of Cu^{2+}, Li^{1+} surface ions normal to the surface.

1. Introduction

$LiCu_2O_2$ continues to attract considerable attention because of the unique physical properties it exhibits. Initially, interest in this system was stimulated by the presence of double-chain ladders of $Cu^{2+}O$, which presented a prototypical quasi-one-dimensional (Q1D) spin-1/2 quantum magnetic system with competing magnetic interactions. Such competing interactions in the classical double-chain ladder were known to give rise to geometric frustration, which in turn is manifest in an ordered incommensurate helimagnetic phase at low temperatures. It was expected that the presence of $S = 1/2$ spins would give rise to strong commensurate quantum spin fluctuations that tend to suppress magnetic order [1–5]. More recently, it was discovered that this system exhibits ferroelectricity upon the emergence of helicoidal magnetic order. This renders $LiCu_2O_2$ as the second cuprate to join the list of multiferroics [6–9].

Electron spin resonance (ESR) measurements revealed the presence of a dimerized spin-singlet ground state at $T > T_N = 24.6$ K, with an energy gap of $\Delta = 72$ K between this state and the first spin-triplet excited state [10]. Below T_N a collinear sinusoidal spin-ordered phase with polarization along the c-axis and a modulation wave vector of $\mathbf{Q} = (0, 0.172, 0)$ r.l.u. was reported [11,12]. A second magnetic phase transition was reported to occur at $T_{FE} \simeq 23.0$ K. Below this temperature, an ordered helicoidal magnetic phase appears, where the spin polarization acquires small components along the a and b axes [1,11,13,12]. The onset of the helicoidal phase induces ferroelectricity with polarization along the c-axis [6,9].

$LiCu_2O_2$ is a quasi-1D insulator. It has a layered charge-ordered orthorhombic crystal structure belonging to the *Pnma* space group; the primitive cell has lattice constants $a = 5.73$ Å, $b = 2.86$ Å, $c = 12.47$ Å respectively [14]. It is a mixed-valent compound with copper ions in the Cu^{2+} and Cu^{1+} valence states. The magnetic Cu^{2+} ($S = 1/2$) ions are located at the center of edge-sharing CuO_4 plaquettes which form infinite chains along the crystallographic b-axis. Coplanar chains are connected by chains of Li ions along the a-axis, and two such planes form double-layers parallel to the ab-plane, as shown in Fig. 1. The Q1D spin arrangement is due to these double-chains of Cu^{2+} ions that run along the crystallographic b axis. The period of each leg of the double spin chains is equal to b. The two legs are offset by b/2 relative to each other. Along the c-axis, each double-layer is separated from its double-layer neighbors by magnetically inert Cu^{1+} planes.

Despite the extensive studies of bulk structural and magnetic properties of $LiCu_2O_2$ crystals cited above, no investigation of its surface properties has been reported in the literature. It is known that $LiCu_2O_2$ crystals easily peel along the (001) surface. However, since these crystals consist of alternating double-layers of $Li^{1+}Cu^{2+}O_2^{2-}$ and single layers of Cu^{1+}, it remains to be determined whether the cleavage would result in the coexistence of $Li^{1+}Cu^{2+}O_2^{2-}$ and Cu^{1+} surfaces, or in an exclusive presence of one of these layer types. If the latter scenario occurs, then it would dictate that the double-layer must split in order to provide complete coverage of the two newly exposed surfaces. The double-layer

* Corresponding author.
E-mail address: elbat@bu.edu (M. El-Batanouny).

0039-6028/$ - see front matter © 2010 Elsevier B.V. All rights reserved.
doi:10.1016/j.susc.2010.01.017

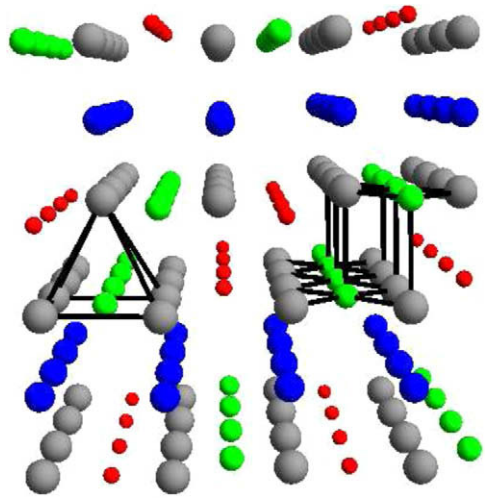

Fig. 1. Crystal structure of $LiCu_2O_2$. The color code is: Li (red), O (gray), Cu^{1+} (blue), Cu^{2+} (green). (For interpretation of the references to colour in this figure legend, the reader is referred to the web version of this article.)

splitting means the splitting of the double-chain and the presence of a single-chain, which is expected to display different magnetic behavior from that observed in the double-chain.

In this paper we present the results of extensive studies of the (001) surface of $LiCu_2O_2$, using the experimental techniques of elastic and inelastic helium scattering aimed at determining its surface structural and dynamical properties, respectively. Furthermore, we used lattice-dynamical models with slab geometries to interpret the surface phonon dispersion curves derived from the measured inelastic scattering spectra. As we will demonstrate below, the surface corrugation topography, derived from a large set of measured diffraction patterns, clearly shows that the surface termination is exclusively $Li^{1+}Cu^{2+}O_2^{2-}$. Moreover, empirical lattice dynamics models, with slab geometries based on such termination and fit to the inelastic experimental results, reveal two low-lying dispersion curves with polarizations normal to the surface, one involves Cu^{2+} and the second involves Li^{1+} ions. In Section 2 the experimental setup and procedures are discussed, and the results and conclusion are presented in Section 3.

2. Experimental setup and procedure

Single crystals of $LiCu_2O_2$ with high Li content of $\simeq 0.99 \pm 0.03$ were grown by the floating-zone method. The Li content was determined accurately through combined iodometric titration and thermogravimetric methods. This ruled out the possibility of chemical disorder between Li and Cu ions. Details of the growth procedures and stoichiometry confirmation are given in Ref. [15]. Typical crystal samples used were about 3 mm × 3 mm × 2 mm in size, with its exposed surface parallel to the *ab*-plane. The crystals were attached to an OFHC copper sample-holder by conductive silver epoxy. A cleaving (peeling) post was attached to the top sample surface in a similar way. The prepared sample-holder was mounted on a sample manipulator equipped with *XYZ* motions as well as polar and azimuthal rotations. The pressure in the Ultra-High Vacuum (UHV) chamber was maintained at 10^{-10} torr throughout the experiment to ensure cleanliness of the sample surface during measurement performance. In situ cleaving under UHV conditions was effected by knocking off the cleaving post. Immediately after cleaving, the quality of the long-range ordering on the surface was confirmed by the appearance of sharp diffraction LEED spots.

A supersonic mono-energetic collimated helium beam, with velocity resolution better than 1.4%, was generated by a nozzle-skimmer assembly and 2mm diameter collimating slits. The average beam velocity was varied by attaching the nozzle reservoir to a closed-cycle helium refrigerator, and controlling the reservoir temperature with the aid of a digital temperature controller (Scientific Instruments Model 9700) and a diode sensor attached to the reservoir. As a result, the beam energy can be varied in the range 65–21 meV by varying the nozzle temperature from 300 K to 110 K, respectively. Polar rotation of the sample was used to vary the incident angle θ_i with respect to the surface normal, while the azimuthal rotation was employed to align the scattering plane along a high-symmetry surface crystallographic direction. The scattered He beam was collected by an angle-resolved detector mounted on a two-axis goniometer, which allows the scattered angle θ_f to be varied independently from θ_i [16], and allows in- and out-of the scattering-plane measurements. The detector [17] is comprised of an electron gun and a multichannel plate (MCP) electron multiplier. The electron gun generates a well-collimated, mono-energetic electron beam crossing the He beam at right angles. The energy of the electron beam is tuned to excite the He atoms to their first excited metastable state (2^3S He^*) upon impact. Deexcitation of a He^* atom at the surface of the MCP leads to the ejection of an electron which generates an electron cascade that is then collected by the anode of the multiplier. By electronically pulsing the electron gun, a gate function is created for time-of-flight (TOF) measurements in the inelastic HAS mode. The details of the detection scheme are given in Ref. [17]. All measurements were performed with the sample surface at room temperature.

By writing the He-atom wave vector as $\mathbf{k} = (\mathbf{K}, k_z)$, where $\mathbf{K}$ is the component parallel to the surface, conservation of momentum and energy for in-the-scattering-plane geometry can be expressed as

$$\Delta\mathbf{K} = \mathbf{G} + \mathbf{Q} = k_f \sin\theta_f - k_i \sin\theta_i, \tag{1}$$

$$\Delta E = \hbar\omega(\mathbf{Q}) = E_f - E_i = \frac{\hbar^2}{2M}(k_f^2 - k_i^2), \tag{2}$$

where subscripts i and f denote incident and scattered beams, respectively, and $\Delta\mathbf{K}$ is the momentum transfer parallel to the surface. $\mathbf{G}$ is a surface reciprocal-lattice vector, $\mathbf{Q}$ is the surface phonon wave vector, and $\hbar\omega(\mathbf{Q})$ is the corresponding surface phonon energy. $E_{i,f} = \hbar^2 k_{i,f}^2/2M$, where M is the mass of a He atom. By eliminating $\mathbf{k}_f$ from the above equations, one obtains the so-called scan curve relations which are the locus of all the allowed $\Delta\mathbf{K}$ and ΔE as dictated by the conservation relations,

$$\Delta E = E_i\left[\left(\frac{\sin\theta_i + \Delta\mathbf{K}/k_i}{\sin\theta_f}\right)^2 - 1\right]. \tag{3}$$

The intersections of these scan curves with the phonon dispersion curves define the kinematically allowed inelastic events for a fixed geometric arrangement. Thus, by systematically changing E_i, θ_i, and θ_f, the entire dispersion curves can be constructed.

3. Results and discussion

3.1. Elastic he scattering and surface structure

Diffraction patterns were collected from many crystal samples at a temperature of 300 K for several scattering conditions:

(1) incident He wave numbers, k_i, in the range 6.42 $Å^{-1}$ and 11.12 $Å^{-1}$,
(2) incident angles, θ_i, between 30° and 50°, and
(3) two high-symmetry azimuthal surface orientations, *a* and *b*, separated by 90°.

As was mentioned above, there are two candidates for the surface termination, which are shown in Fig. 2, the $Li^{+1}Cu^{2+}O_2^{2-}$ layer and the Cu^{1+} layer. The former has a rectangular lattice, while the

latter has a square lattice (C_{4v} symmetry) with lattice constant $b \simeq 2.86$ Å. We note that the diffraction peaks that correspond to odd multiples of $2\pi/a$ should be absent for pure Cu^{1+} surface termination, which contradicts the fact that they do appear in all the measured diffraction patterns. Moreover, the Cu^{1+} layer has a high-symmetry direction along the $\langle 11\rangle$-direction in addition to the $\langle 10\rangle$- and $\langle 01\rangle$-directions it shares with the $Li^{1+}Cu^{2+}O_2^{2-}$ layer. Alternatively, for $Li^{1+}Cu^{2+}O_2^{2-}$ termination, the well known crystal twinning [1,6,9] would imply that the two high-symmetry azimuthal orientations would give the same diffraction pattern. This means that we obtain a superposition of diffraction patterns from **a** $\langle 10\rangle$ and **b**$\langle 01\rangle$ directions. Moreover, since for $LiCu_2O_2$ $a \simeq 2b$, the diffraction peaks associated with the b-direction will lie very close to the even-order peaks obtained for the a-direction.

Fig. 3 shows a typical diffraction pattern recorded for $k_i = 7.28$ Å^{-1} and $\theta_i = 31.4°$. Although the twinning makes the situation a little complicated, luckily, the angular resolution in the diffraction pattern allows us to clearly separate the peak positions along the two directions, as indicated by peaks (2,0) and (0,1) in Fig. 3. No discernible diffraction peaks were found along the $\langle 11\rangle$-direction, despite the fact that an appreciable corrugation would be expected from the Cu^{1+} layer along that direction, given a Cu^{1+} ionic radius of ≃0.75 Å and an inter-ionic distance larger than 4 Å. Moreover, we note that the surface layer-stacking, shown in Fig. 2 for a $Li^{1+}Cu^{2+}O_2^{2-}$ termination presents a zero net electric dipole moment in the surface region, while a layer-stacking for the Cu^{1+} termination carries a net electric dipole moment at the sur-

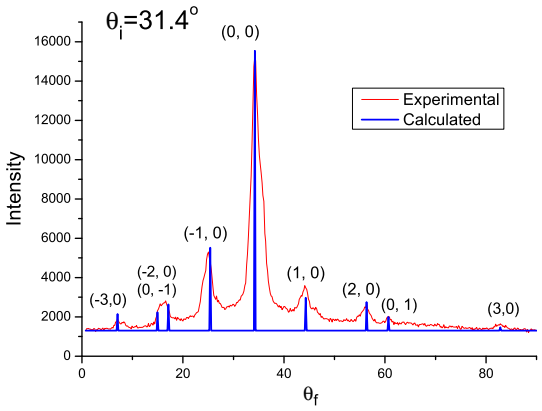

Fig. 3. A typical experimental diffraction pattern with $k_i = 7.28$ Å^{-1}, $\theta_i = 31.4°$ at $T = 300$ K (red), together with the calculated diffraction intensities (blue vertical bars). (For interpretation of the references to colour in this figure legend, the reader is referred to the web version of this article.)

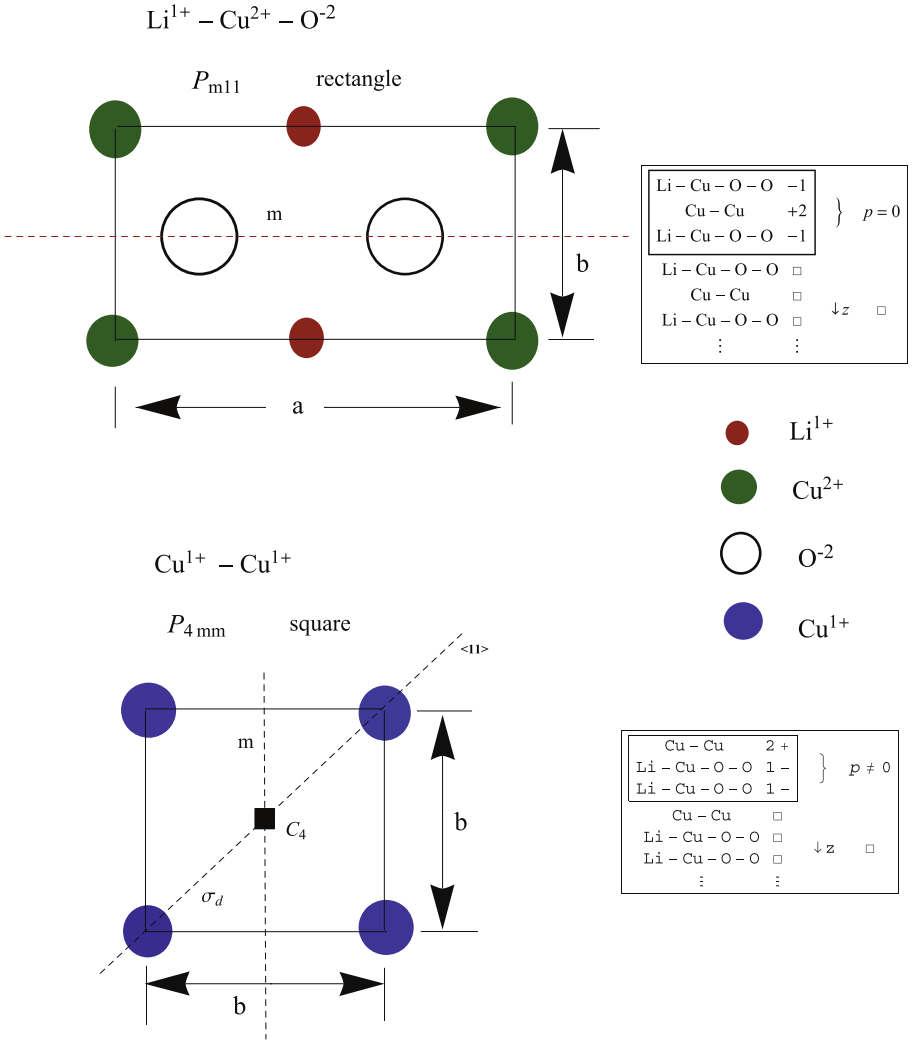

Fig. 2. Top: $Li^{1+}Cu^{2+}O_2^{2-}$ surface termination. Bottom: Cu^{1+} surface termination. Their respective unit cell and layer-stacking are shown in the left and right panels, respectively.

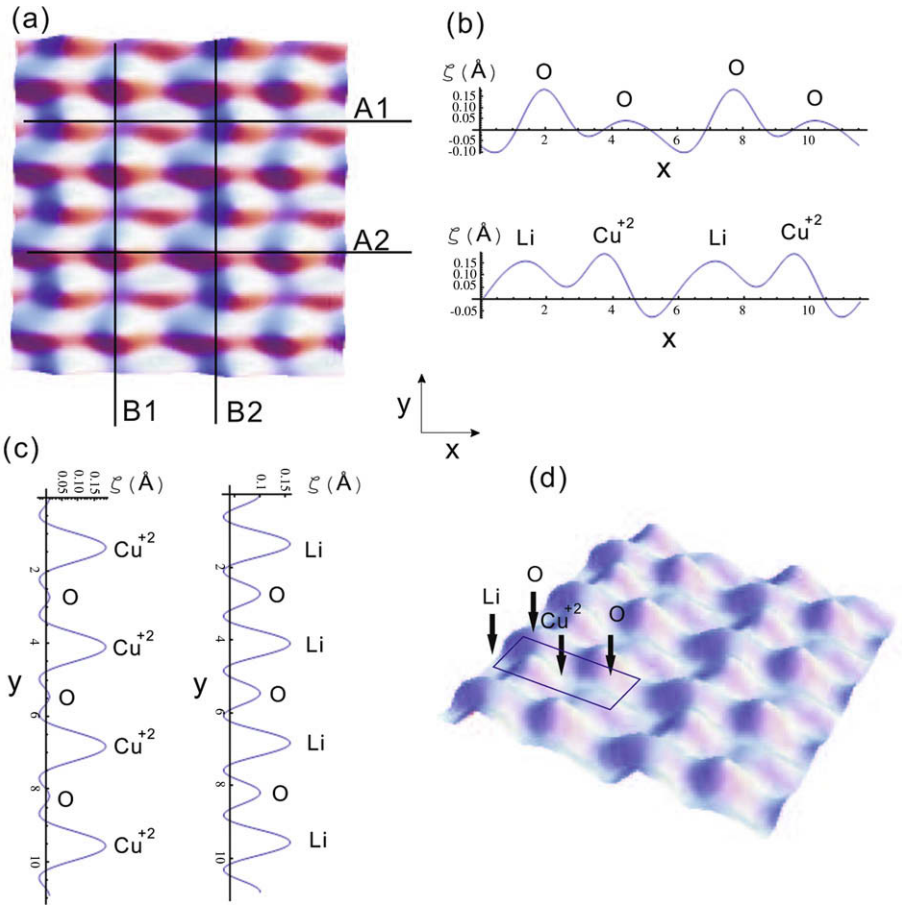

Fig. 4. Calculated surface corrugation function. (a) top view with four cut lines; (b) corrugation of two cut lines (A1, A2) along the *a*-direction; (c) corrugation of two cut lines (B1, B2) along the *b*-direction; (d) perspective view of the corrugation.

face indicating its instability. The instability of a Cu^{1+} surface termination is also corroborated by an equilibrium analysis we carried out for both surface terminations – a prerequisite for lattice dynamics calculations: Whereas equilibrium was achieved for a $Li^{1+}Cu^{2+}O_2^{2-}$ surface termination by a very small upward displacement of the Cu^{2+} rows, we found that the equilibrium of the Cu^{1+} termination cannot be achieved without a radical ionic rearrangement of the top two layers. The equilibrium analysis will be discussed below in more detail. Given all these facts, we are inclined to rule out the presence of a Cu^{1+} termination or the coexistence of both surface terminations. Hence, we shall follow the scenario of a purely $Li^{1+}Cu^{2+}O_2^{2-}$ termination.

The surface periodicity along **a** and **b** is derived from the positions of their corresponding diffraction peaks using the relation

$$|\mathbf{k_i}|(\sin\theta_i - \sin\theta_{\mathbf{G}}) = |\mathbf{G}|, \tag{4}$$

where $\mathbf{k_i}$ is the incident beam wave vector, **G** a surface reciprocal-lattice vector, $\theta_{\mathbf{G}}$ the corresponding scattering angle. Analysis of all the collected diffraction patterns yields the surface lattice constant values: $a_s = 5.76 \pm 0.05$ Åand $b_s = 2.91 \pm 0.08$ Å, which compares quite well with the bulk values of $a = 5.73$ Å, $b = 2.86$ Å and, thus, precludes the presence of diffraction satellites and surface reconstruction.

In order to determine the topology of the surface primitive cell we used the *hard corrugated wall model* within the *eikonal approximation* to calculate the elastic scattering intensities [18]. Here, the surface topology is defined in terms of a surface corrugation function $\zeta(\mathbf{R})$ [19], where **R** denotes a surface position vector and ζ the corrugation height at that position. In this framework, the scattering amplitude of the diffraction peak **G** is given by [19]

$$A_{\mathbf{G}} = -\frac{1}{S}\int_{\text{u.c.}} e^{i[\mathbf{G}\cdot\mathbf{R}+q_{Gz}\zeta(\mathbf{R})]}d\mathbf{R}, \tag{5}$$

where $q_{Gz} = k_{iz} - k_{Gz}$, with $k_{Gz} = k_i\cos\theta_{\mathbf{G}}$. The integration is carried over the unit cell (u.c.) of area *S*. Since $\zeta(\mathbf{R})$ should have the surface periodicity, we write

$$\zeta(\mathbf{R}) = \sum_{\mathbf{G}} \zeta_{\mathbf{G}}\exp(i\mathbf{G}\cdot\mathbf{R}). \tag{6}$$

We make use of the reflection symmetry perpendicular to the *b*-direction (*y*-axis) of the $LiCu_2O_2$ surface to simplify Eq. (6), and write

$$\zeta(x,y) = \sum_{n_1,n_2}\zeta_{n_1,n_2}\sin(n_1b_1x)\cos(n_2b_2y) + \sum_{n_3,n_4}\zeta_{n_3,n_4}\cos(n_3b_1x)\cos(n_4b_2y), \tag{7}$$

where $b_1 = \frac{2\pi}{a}, b_2 = \frac{2\pi}{b}$, are the surface reciprocal-lattice vector basis.

The goal now is to determine the coefficients $\zeta_{\mathbf{G}}$. The following iterative fitting scheme was adopted [20]: Initially, the magnitudes $|A_{\mathbf{G}}|$ are determined from the experimental diffraction pattern using the geometric relation

$$P_{\mathbf{G}} = \frac{|k_{Gz}|}{|k_{iz}|}|A_{\mathbf{G}}|^2, \tag{8}$$

where $P_{\mathbf{G}}$ is the intensity of the **G** diffraction peak. The experimental intensities were normalized to satisfy the unitarity condition

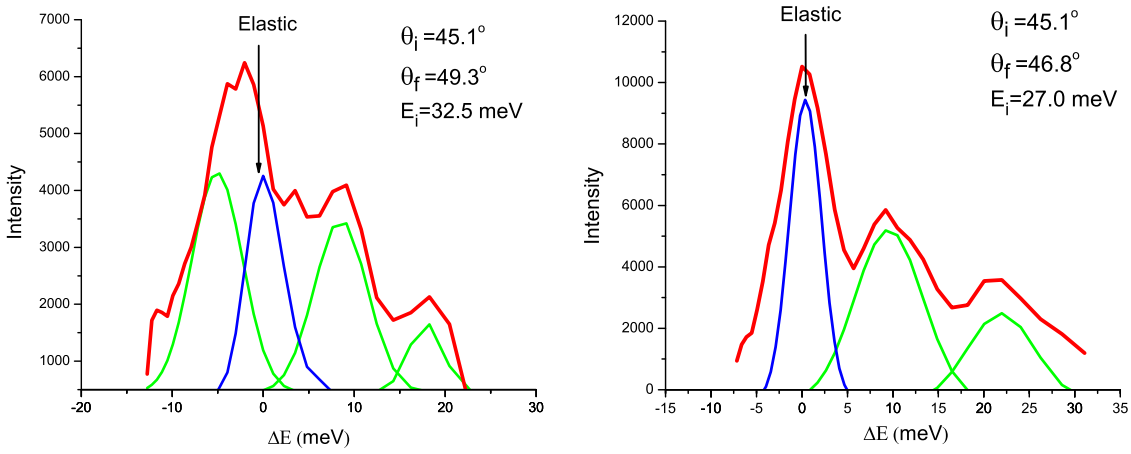

Fig. 5. Typical time-of-flight spectra. The experimental curve (red) is resolved into inelastic peaks (green) and the diffuse elastic peak (blue), which is also indicated by arrows. (For interpretation of the references to colour in this figure legend, the reader is referred to the web version of this article.)

$$\sum_{\mathbf{G}} P_{\mathbf{G}} = 1. \tag{9}$$

Next, the eikonal equation [18–20]

$$\sum_{\mathbf{G}} A_{\mathbf{G}} e^{i\mathbf{G}\cdot\mathbf{R}} e^{ik_{G_z}\zeta(\mathbf{R})} = -e^{ik_{iz}\zeta(\mathbf{R})}, \tag{10}$$

where $A_{\mathbf{G}} = |A_{\mathbf{G}}|e^{i\phi_{\mathbf{G}}}$, is used to determine $\zeta(\mathbf{R})$. $\phi_{\mathbf{G}}$ is a diffraction phase angle to be determined. In the first iteration we set $A_{\mathbf{G}} = |A_{\mathbf{G}}|$, which yields

$$\zeta_0(\mathbf{R}) = \frac{\ln\left(-\sum_{\mathbf{G}} A_{\mathbf{G}} e^{i\mathbf{G}\cdot\mathbf{R}}\right)}{2ik_{iz}},$$

where we replaced k_{G_z} by $-k_{iz}$ in Eq. (10). Further iterations involved varying the amplitudes $\zeta_{\mathbf{G}}$ around the values obtained from $\zeta_0(\mathbf{R})$.

After each iteration a reliability factor R

$$R = \frac{1}{N}\sqrt{\sum_{\mathbf{G}} (P_{\mathbf{G}}^{\exp} - P_{\mathbf{G}}^{\mathrm{calc}})^2}, \tag{11}$$

was calculated. N is the number of diffraction peaks. The iterations were terminated at $R = 0.003$, yielding calculated diffraction peak intensities shown as blue vertical bars in Fig. 3, and an intensity sum of 0.981; which is very close to the unitarity condition (9). It gave the corrugation function

$$\begin{aligned}\zeta(x,y) = &-0.06\cos(b_1x) - 0.05\cos(2b_1x) + 0.02\cos(3b_1x)\\ &+ 0.03\sin(b_1x) - 0.03\cos(b_2y) + 0.05\cos(2b_2y)\\ &- 0.07\cos(b_2y)\sin(2b_1x),\end{aligned} \tag{12}$$

where the coefficients are given in Å. It is plotted in Fig. 4.

The locations of the Li^{1+}, Cu^{2+},and the two O^{2-} ions were identified by comparing the positions of the corrugation maxima to ionic positions in the unit cell, and are indicated in panels (b)–(d) of Fig. 4. Moreover, we find from panels (b) and (c) that the peak-to-peak corrugations are about 0.25 Å and 0.16 Å along the a and b directions, respectively, which are less than 6% of the corresponding lattice parameters.

3.2. Inelastic measurements and shell-model calculations

Inelastic scattering measurements were carried out for in-the-scattering-plane geometry. Two typical TOF spectra, showing diffuse elastic as well as inelastic peaks, are presented in Fig. 5. The data were collected using beam energies in the range of 25–65 meV. The high-energy He beam, $E_i = 65$ meV, was used to probe the high-frequency surface phonon modes. The energy resolution for the lowest-energy beam was about 3 meV. Spectral peaks were identified in TOF spectra with the aid of Gaussian fitting; and phonon energies and momenta were calculated from the TOF peak

Table 1
Best-fit Born–Meyer and shell parameters.

Born–Meyer potential parameters				Shell model parameters			
Bond	a (eV)	b (Å^{-1})	c (eV Å^6)	Ion	Z (e)	Y (e)	K (eV/Å^2)
Cu^{1+}–O	18705.6	2.9	–	Li	+1	1.5	5
Cu^{2+}–O	10000	4.4	–	Cu^{1+}	+1	1.7	20
Cu^{1+}–Cu^{2+}	3490.95	3.0	–	Cu^{2+}	+2	2.9	30
Cu^{1+}–Cu^{1+}	18853	3.0	–	O[b]	−2	−3.1	40
Cu^{2+}–Cu^{2+}	6598.44	3.0	–				
O–O	2146.30	3.4	50				
Li–O[a]	840	3.0	–				

[a] Ref. [21].
[b] Ref. [16].

Table 2
Comparison of experimental and calculated Raman and IR frequencies.

Mode	Polarization	Frequency (cm^{-1})	
		Experiment [5]	Calculated
Raman active			
A_g	aa	573	593.30
		497	–
		460	476.76
		367	375
		297	275.9
		178	191.33
		167	–
		122	108.86
		Experiment [23]	Calculated
IR active			
B_{2u}	b	240	–
		288	268.79
		312	–
		416	449.88
B_{3u}	a	240	222.88
		288	269.621
		320	–
		392	375.54
		440	463.08/474.46

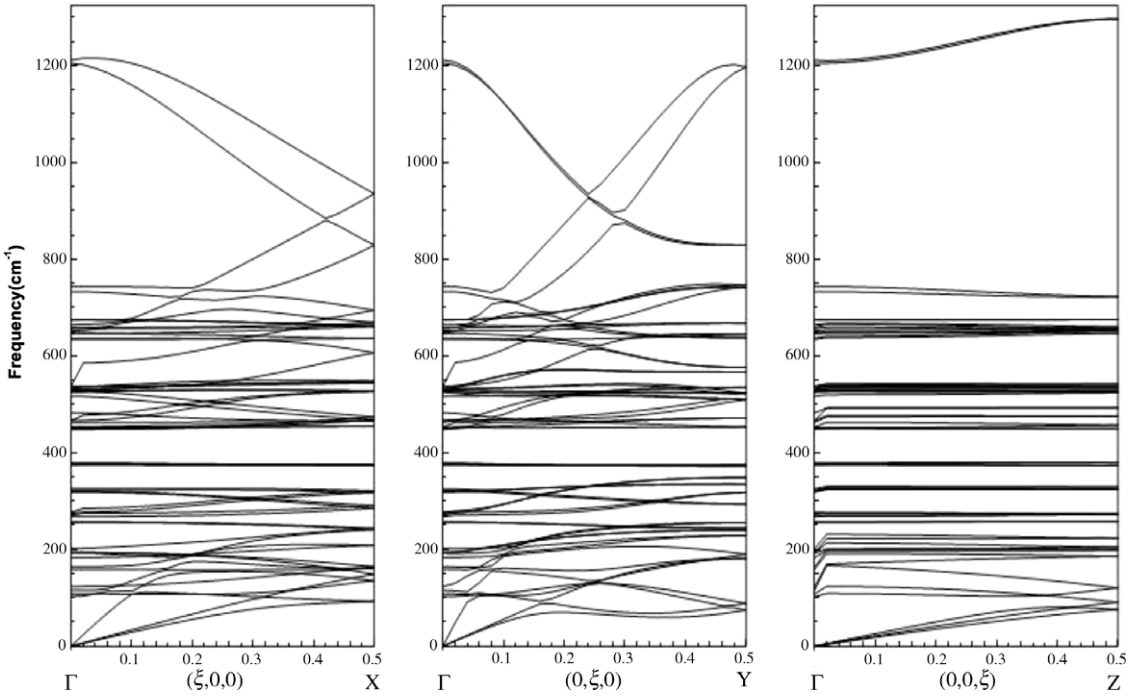

Fig. 6. Bulk phonon dispersion curves along **a** ($\xi = q/G_a$), **b** ($\xi = q/G_b$) and **c** ($\xi = q/G_c$).

positions using Eqs. (1) and (2). To characterize the ensuing phonon dispersion points, empirical lattice-dynamical analysis for the bulk and surface (slab calculations) was carried out.

3.2.1. Static equilibrium and bulk lattice dynamics

Phonon dispersion curves obtained from bulk lattice dynamics calculations, based on the shell-model, were empirically fit to

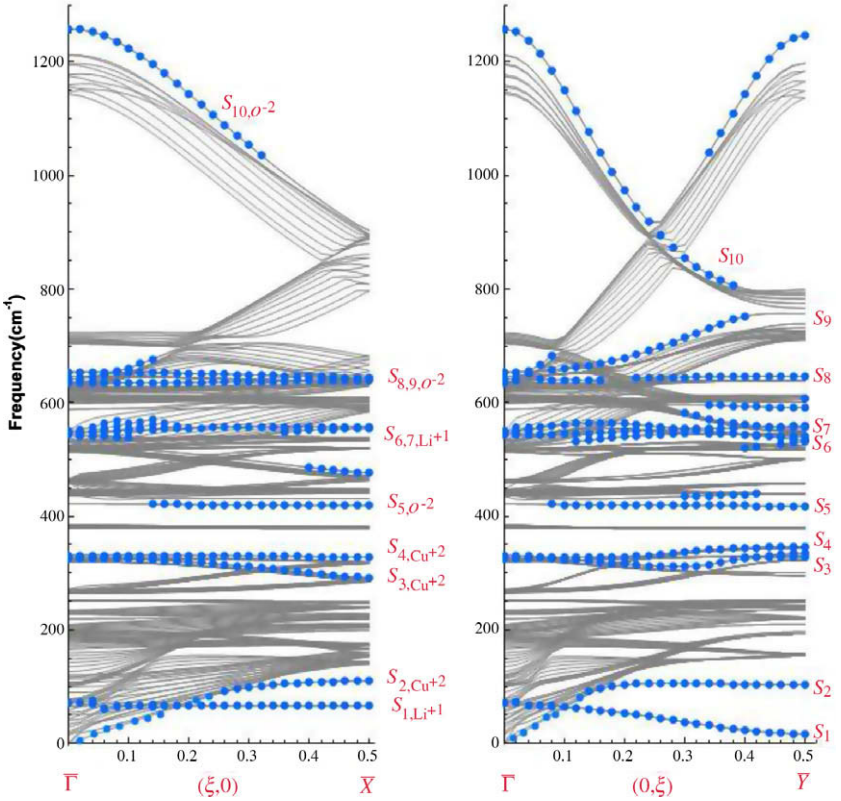

Fig. 7. Surface phonon dispersion curves, indicated by blue dots superimposed on a gray background. The latter represents the surface projection of bulk bands on the surface BZ. The surface modes are labeled S_i, $i = 1, \ldots, 10$.

Table 3
Character of the surface phonon dispersion curves. (Pol.: polarization, AP: anti-phase, IP: in-phase).

Branch	⟨10⟩		⟨01⟩		Type
	Ions	Pol.	Ions	Pol.	
S_1	Li^{1+}	z	Cu^{2+}, Li^{1+} 1 : 5	z	AP (⟨01⟩)
S_2	Cu^{2+}	z	Cu^{2+}, Li^{1+} 5 : 1	z	IP (⟨01⟩)
S_3	Cu^{2+}	y	Cu^{2+}	x	
S_4	Cu^{2+}	x	Cu^{2+}	y	
S_5	O^{2-}	z	O^{2-}	z	
S_6	Li^{1+}	y	Li^{1+}	x	
S_7	Li^{1+}	x	Li^{1+}	y	
S_8	O^{2-}	y	O^{2-}	x	IP
S_9	O^{2-}	y	O^{2-}	y	AP
S_{10}	O^{2-}	x	O^{2-}	x	AP

existing IR and Raman data. In lattice-dynamical studies of complex systems such as $LiCu_2O_2$, the construction of a dynamical matrix based on pair potentials rather than mere force constants is far more advantageous in the sense that the underlying physics is transparent and many of the potential parameters for similar pair interactions can be transferred from one compound to another. This is especially useful when experimental phonon frequencies are limited to a few bulk infrared (IR) and Raman active phonon modes at the center of the Brillouin zone (BZ) [16,21], and no neutron-scattering data for phonon dispersion is available.

The model we employ in the present calculations incorporates two-body central potentials, namely the Coulomb potential $V_{ij}^{C}(r) = Z_i Z_j e^2/r$ for the long-range interactions, and either Born–Mayer $V_{ij}(r) = a_{ij}e^{-b_{ij}r}$ or Buckingham $V_{ij}(r) = a_{ij}\exp(-b_{ij}r) - c_{ij}/r^6$ potentials for short-range interactions. Some of the initial values of the parameters of the short-range pair potentials were obtained from the literature: (Cu^{2+}–O) [16], (O–O) [16] and (Li–O) [21]. The remaining pair potential parameters were set to satisfy the static equilibrium conditions [22] which require that the forces acting on the ions in their equilibrium positions should vanish. This treatment also ensures the consistency of the static and dynamical properties of the crystal. It should be noted that satisfying static equilibrium conditions is a prerequisite for lattice dynamics calculations, however, it does not guarantee dynamical stability, which requires reality of the phonon frequencies throughout the BZ.

Moreover, in the shell-model, the ions are characterized by ionic charge Z, shell charge Y, and intra-ion shell-core force constant K. It should also be noted that the shell-model parameters do not appear in the static equilibrium equations where ions are treated as rigid bodies. However, these parameters are introduced into the dynamical matrix and are determined through the process of fitting the 17 experimental IR and Raman modes reported in the literature. The short-range potential and shell-model parameters that produce the best fit for these modes are listed in Table 1.

According to the point group *mmm* (D_{2h}) of the space group *Pnma*, there are 30 Raman active and 22 IR active modes at the Γ-point. They are classified in terms of the corresponding irreducible representations as

$$10A_g \oplus 5B_{1g} \oplus 10B_{2g} \oplus 5B_{3g} \quad \text{Raman}$$
$$9B_{1u} \oplus 4B_{2u} \oplus 9B_{3u} \quad \text{IR}$$

A comparison of the experimental and calculated values of these modes is given in Table 2.

The remaining modes at the Γ-point include five A_u modes and three zero-frequency acoustic modes. The identification of the symmetries of the calculated modes at the Γ-point was established with the aid of the symmetry projection operators [24] of the point group *mmm*.

Away from the Γ-point, the point group of the wave vector is isomorphic with C_{2v} for all three high-symmetry directions. Symmetry compatibility relations give

C_{2v}	D_{2h}		
	$\Delta(\langle 100\rangle)$	$\Sigma(\langle 010\rangle)$	$\Lambda(\langle 001\rangle)$
A_1	A_g	A_g	A_g
	B_{3u}	B_{2u}	B_{1u}
A_2	A_u	A_u	A_u
	B_{3g}	B_{2g}	B_{1g}
B_1	B_{1g}	B_{1g}	B_{3g}
	B_{2u}	B_{3u}	B_{2u}
B_2	B_{2g}	B_{3g}	B_{2g}
	B_{1u}	B_{1u}	B_{3u}

The complete set of calculated bulk phonon dispersion curves (60 branches) that gives the best fit to experimental data is shown in Fig. 6, along the high-symmetry directions Γ–X (a-direction), Γ–Y (b-direction) and Γ–Z (c-direction). In all, we have $20A_1 \oplus 10A_2 \oplus 10B_1 \oplus 20B_2$ along the ⟨100⟩- and the ⟨001⟩-directions, and $15A_1 \oplus 15A_2 \oplus 15B_1 \oplus 15\ B_2$ along the ⟨010⟩-direction.

The highest two bands ($\simeq$ 800–1200 cm^{-1}) are longitudinal optic phonons involving the motion of the eight O^{2-} ions in the primitive cell; in the upper band the four O1 ions at positions {0.137, 1/4, 0.405}, {0.363, 3/4, 0.905}, {0.863, 3/4, 0.595}, {0.637, 1/4, 0.095} move in-phase with each other, but anti-phase with the four O2 ions at positions {0.115, 1/4, 0.105}, {0.385, 3/4, 0.605}, {0.885, 3/4, 0.895}, {0.615, 1/4, 0.395}, while in the lower band, the O1 and O2 ions still have anti-phase motion, but also the ions at $y = 1/4$ have anti-phase motion with those at $y = 3/4$. The lowest three bands (acoustic phonons) mix with higher bands at higher **q** vectors in the a- and b-directions, but remain distinct in the c-direction.

3.2.2. Slab-geometry lattice dynamics and surface phonons

Surface equilibrium analysis for a Cu^{1+} termination revealed that bulk-like positions for the top two layers suffer from large electrostatic forces that tend to displace the Cu^{1+}, Li^{1+} and Cu^{2+} ions inwards while pushing the O^{2-} ions outwards, signaling the onset of a drastic reconstruction which, in turn, deems a lattice dynamics calculations for such termination to be unrealistic.

By contrast, a surface equilibrium analysis for a $Li^{1+}Cu^{2+}O_2^{2-}$ termination showed that the Cu^{2+} surface ions have to be displaced outward, along the surface normal, from their bulk positions, in order to satisfy equilibrium conditions in that direction. The pair potential and shell-model parameters of Table 1 were used in the initial slab calculations. However, the surface parameters had to be modified in order to achieve global stability in the entire surface BZ.

A lattice dynamics shell-model with slab-geometry consisting of 36 layers, and terminated with $Li^{1+}Cu^{2+}O_2^{2-}$ surfaces, was used to calculate the corresponding surface phonon dispersion curves. Since translation symmetry is broken normal to the slab surfaces, primitive and non-primitive translations along this direction are not allowed. Consequently, the slab symmetry reduces to *2ma*, while the surface symmetry is *p1m*.

The resulting surface phonon dispersion curves are shown as blue dots superimposed on a gray background in Fig. 7; they are labeled $S_i,\ i = 1, \ldots, 10$. The gray background areas and lines resulting from the slab calculations correspond to contributions from the slab bulk, namely projections onto the surface BZ. Some of the dispersed gray lines would turn into solid bands as the thickness of the slab approaches infinity. The general character of the surface

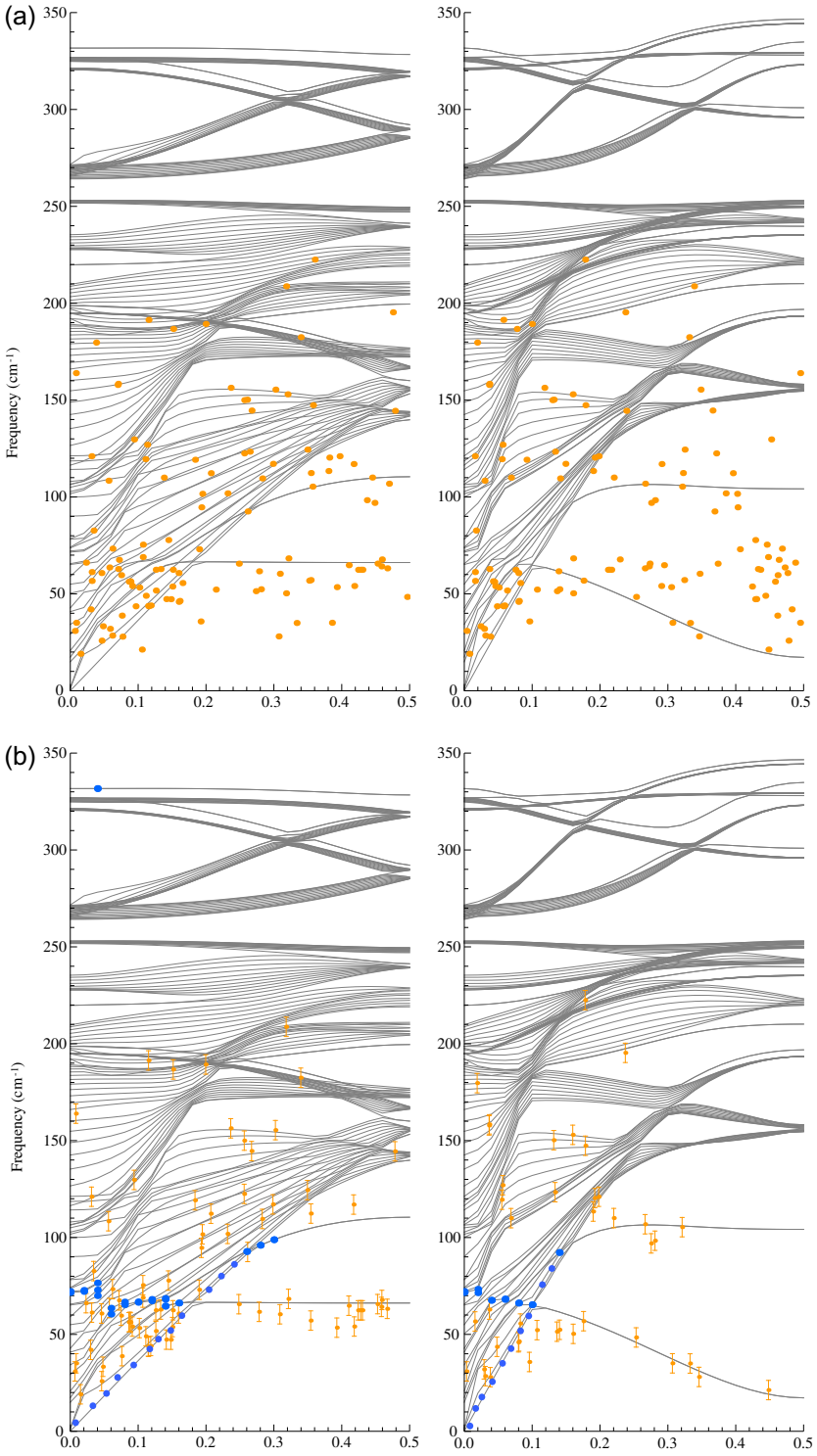

Fig. 8. (a) All measured inelastic events, reduced to the proper surface *BZ*, superposed on calculated dispersion curves along ⟨10⟩, (left panel), and ⟨01⟩ (right panel). (b) Fits obtained by the procedure described in the main text for ⟨10⟩, (left panel), and ⟨01⟩ (right panel). (Error bars are also indicated in the lower panels).

modes $S_1 - S_{10}$ is given in Table 3. S_1 and S_2 involve the motions of the Cu^{2+} and Li^{1+} normal to the surface.

While S_1 is quite flat for wave vectors $q \simeq 0.15$–$0.5(2\pi/a)$ along the *a*-direction, it exhibits anomalous softening in the proximity of the surface BZ boundary along the *b*-direction. This softening could be the result of the tenuous equilibrium of these ions normal to the surface.

The scattering of He beams with energies in the range 25–65 meV allows measurement of surface phonons with frequencies below 400 cm^{-1} (50 meV). Thus we will focus on identifying the measured inelastic scattering events with calculated surface phonon dispersion curves in that range. The process of identification is further complicated by the presence of twining in the sample crystals. A successful procedure must be capable of sorting out modes propagating in the *a*-direction from those propagating in the *b*-direction. Fig. 8a illustrates this complexity. Here, all measured inelastic events are plotted in the left and right panels, after reducing their momenta to the first surface *BZ* along the *a*-direc-

tion (left panel) and along the *b*-direction (right panel). Notice that each measured inelastic event has a different value of its reduced momentum for the different directions. The sorting criterion adopted, was to assign a given event to the direction where it is nearest in energy to a dispersion curve. The final result is plotted in Fig. 8b. The agreement is surprisingly quite good, especially with the two low-lying dispersion curves. In addition, this agreement supports the surface termination analyzed in this paper.

4. Conclusion

With the aid of He scattering techniques at room temperature, we find that the (0 0 1) surface of $LiCu_2O_2$ is exclusively terminated by $Li^{1+}Cu^{2+}O_2^{2-}$, and that no surface reconstruction occurs. Empirical fitting of lattice dynamics, shell-model based, calculations to measured inelastic He scattering spectra, supports the proposed termination and reveals that the lowest surface phonon dispersion branches involve the motion of Cu^{2+} and Li^{1+} ions normal to the surface.

Acknowledgments

This work is supported by the US Department of Energy under Grant No. DE-FG02-85ER45222. FCC acknowledges the support from the National Science Council of Taiwan under project number NSC-95-2112-M-002.

References

[1] T. Masuda, A. Zheludev, A. Bush, M. Markina, A. Vasiliev, Phys. Rev. Lett. 92 (2004) 177201.
[2] T. Masuda, A. Zheludev, B. Roessli, A. Bush, M. Markina, A. Vasiliev, Phys. Rev. B 72 (2005) 014405.
[3] L. Mihály, B. Dóra, A. Ványolos, H. Berger, L. Forró, Phys. Rev. Lett. 97 (2006) 067206.
[4] A.A. Gippius, E.N. Morozova, A.S. Moskvin, A.V. Zalessky, A.A. Bush, M. Baenitz, H. Rosner, S.-L. Drechsler, Phys. Rev. B 70 (2004) 020406.
[5] K.-Y. Choi, S.A. Zvyagin, G. Cao, P. Lemmens, Phys. Rev. B 69 (2004) 104421.
[6] S. Park, Y.J. Choi, C.L. Zhang, S.-W. Cheong, Phys. Rev. Lett. 98 (2007) 057601.
[7] H.J. Xiang, M.-H. Whangbo, Phys. Rev. Lett. 99 (2007) 257203.
[8] S.W. Huang, D.J. Huang, J. Okamoto, C.Y. Mou, W.B. Wu, K.W. Yeh, C.L. Chen, M.K. Wu, H.C. Hsu, F.C. Chou, C.T. Chen, Phys. Rev. Lett. 101 (2008) 077205.
[9] S. Seki, Y. Yamasaki, M. Soda, M. Matsuura, K. Hirota, Y. Tokura, Phys. Rev. Lett. 100 (2008) 127201.
[10] S. Zvyagin, G. Cao, Y. Xin, S. McCall, T. Caldwell, W. Moulton, L.-C. Brunel, A. Angerhofer, J.E. Crow, Phys. Rev. B 66 (2002) 064424.
[11] A. Rusydi, I. Mahns, S. Müller, M. Rübhausen, S. Park, Y.J. Choi, C.L. Zhang, S.-W. Cheong, S. Smadici, P. Abbamonte, M.v. Zimmermann, G.A. Sawatzky, Appl. Phys. Lett. 92 (2008) 262506.
[12] Y. Kobayashi, K. Sato, Y. Yasui, T. Moyoshi, M. Sato, K. Kakurai, J. Phys. Soc. Jpn. 78 (2009) 084721.
[13] Y. Yasui, K. Sato, Y. Kobayashi, M. Sato, J. Phys. Soc. Jpn. 78 (2009) 084720.
[14] R. Berger, J. Alloys Compd. 184 (1992) 315.
[15] H.C. Hsu, H.L. Liu, F.C. Chou, Phys. Rev. B 78 (2008) 212401.
[16] M. Farzaneh, X.-F. Liu, M. El-Batanouny, F.C. Chou, Phys. Rev. B 72 (2005) 085409.
[17] K. Martini, W. Franzen, M. El-Batanouny, Rev. Sci. Instrum. 58 (1987) 1027.
[18] D. Farias, K.-H. Rieder, Rep. Prog. Phys. 61 (1998) 1575.
[19] U. Garibaldi, A. Levi, R. Spadacini, G. Tommei, Surf. Sci. 48 (1975) 649.
[20] K. Rieder, N. Garcia, V. Celli, Surf. Sci. 108 (1981) 169.
[21] R.A. Jackson, M.E. Valerio, J. Phys.: Condens. Matter 17 (2005) 837.
[22] D.A. Zatsepin, V.R. Galakhov, M.A. Korotin, V.V. Fedorenko, E.Z. Kurmaev, S. Bartkowski, M. Neumann, R. Berger, Phys. Rev. B 57 (1998) 4377.
[23] M. Papagno, D. Pacilé, G. Caimi, H. Berger, L. Degiorgi, M. Grioni, Phys. Rev. B 73 (2006) 115120.
[24] M. El-Batanouny, F. Wooten, Symmetry and Condensed Matter Physics: A Computational Approach, Cambridge University Press, 2008.